PHYSICAL REVIEW E **107**, 014801 (2023)

Nanoscale pattern formation produced by ion bombardment of a rotating target: The decisive role of the ion energy

R. Mark Bradley
Departments of Physics and Mathematics, Colorado State University, Fort Collins, Colorado 80523, USA

Daniel A. Pearson [*]
Division of Science and Engineering, Pennsylvania State University, Abington, Abington, Pennsylvania, 19001, USA

(Received 27 October 2022; accepted 3 January 2023; published 17 January 2023)

We study the nanoscale patterns that form on the surface of a rotating sample of an elemental material that is bombarded with a broad noble gas ion beam for angles of incidence θ just above the critical angle for pattern formation θ_c. The pattern formation depends crucially on the ion energy E. In simulations carried out in the low-energy regime in which sputtering is negligible, we find disordered arrays of nanoscale mounds (nanodots) that coarsen in time. Disordered arrays of nanodots also form in the high-energy regime in which there is substantial sputtering, but no coarsening occurs close to the threshold angle. Finally, for values of E just above the sputter yield threshold, nanodot arrays with an extraordinary degree of hexagonal order emerge for a range of parameter values, even though there is a broad band of linearly unstable wavelengths. This finding might prove to be useful in applications in which highly ordered nanoscale patterns are needed.

DOI: 10.1103/PhysRevE.107.014801

I. INTRODUCTION

Bombardment with a broad ion beam is a widely employed means of producing nanoscale patterns on solid surfaces [1]. A variety of patterns, including surface ripples and arrays of nanodots or nanoholes, can be fabricated in a single process step without using a mask or photoresist [1–11]. Nanoscale surface ripples, in particular, will form on virtually any solid target material if the angle of ion incidence θ exceeds a critical value. The formation of ripples, however, is undesirable in various applications in which solids are bombarded with broad ion beams, e.g., secondary ion mass spectroscopy (SIMS), Auger electron spectroscopy (AES), and ion milling. In the simplest kind of SIMS or AES apparatus, the primary ions are obliquely incident on the stationary surface of the sample. As sputtering proceeds, ripples can form, and this leads to rapid degradation of the depth resolution.

Zalar demonstrated that this problem can often be overcome by rotating the sample with a constant angular velocity about its surface normal as the depth profiling proceeds [12]. Zalar rotation has subsequently been used by numerous other groups, who found that in many cases the surface actually becomes flatter as the solid is eroded [13]. As a result, ion sputtering with concurrent sample rotation has also been used as a means of preparing ultrasmooth surfaces for optical applications [14].

If the angle of ion incidence θ exceeds a critical value θ_c that depends on the target material and the choice of ion species and energy, sample rotation does not prevent surface roughening and nanoscale patterns form [13,15,16]. A theory that describes the time evolution of the surface of a rotating sample that is sputtered by a broad ion beam was advanced by Bradley and Cirlin [17]. This theory applies only in the early-time, linear regime. Subsequently, Bradley [18] incorporated nonlinear terms into the theory and found that the equation of motion (EOM) is the isotropic Kuramoto-Sivashinsky (KS) equation to a good approximation if θ exceeds θ_c and the rotational angular velocity ω is sufficiently large [19]. The surface roughness asymptotes to a finite steady-state value and the topography is a disordered array of mounds in that event. In the opposite limit of slow rotation, Bradley argued that if the surface is unstable, ripples with their wave vector lying parallel to the projected beam direction will be present in the steady state. This has since been confirmed by experiments and simulations [20].

Experimental studies of the nanoscale patterns produced by ion bombardment of stationary and rotating targets have typically been done with noble gas ions that have energies on the order of 1 keV. In this regime, sputter yields are normally of order unity. For a given target material, ion species, and angle of incidence, the feature size of the nanostructures is found to be an increasing function of the ion energy [1]. To produce smaller feature sizes, therefore, ions of lower energy should be employed.

When the energy of the incident ions is on the order of a few tens of electron volts, sputtering is negligible. Experiments in this low-energy regime are few and all have been done with a stationary target. These experiments reveal that nanoscale patterns do form: surface ripples as well as disordered arrays of nanostructures elongated along the projected beam direction have been observed [21–24]. In addition to its intrinsic scientific interest, the low-energy regime may become important in applications since the feature size of the nanostructures can be below 50 nm.

---

[*] Corresponding author: dap5063@psu.edu

In the low-energy regime, mass redistribution (MR) takes place: momentum transfer from the incident ions to atoms near the solid surface leads to inelastic displacement of the atoms [25–27]. Depending on the ion energy and target material, dozens of atoms can be displaced even though there is essentially no sputtering. MR is important at ion energies on the order of 1 keV, a regime in which sputter yields are relatively high [28]. It plays an even more crucial role in the low-energy regime in which sputtering is negligible [24].

Ions can be implanted in the low-energy regime. However, when an ion is incident on the solid surface, the result can be at most one implanted ion whereas, as noted above, dozens of atoms can be displaced. In addition, noble gas ions penetrate only a few nanometers into the solid, are highly mobile, and usually desorb when they reach the solid surface [29]. Implantation of noble gas ions can therefore be neglected [30]. This is confirmed by estimates of the curvature coefficients in the linearized EOM obtained using molecular dynamics simulations and the crater function formalism [24].

When sputtering and implantation are neglected, the mass of the solid is conserved. This makes the low energy limit fundamentally different than the higher energy regime in which sputtering is significant. The EOM that is valid for a rotating target in the high energy regime, the isotropic KS equation [18], cannot be valid in the low energy regime because it does not conserve mass. In addition, while MR and curvature-dependent sputtering can both contribute to the surface instability in the high energy regime, the instability is entirely due to MR in the low-energy regime.

In this paper, we will study the patterns formed on the surface of a rotating sample of an elemental material that is bombarded with a noble gas ion beam for angles of incidence θ just above the critical angle for pattern formation θ_c. The EOM can be rigorously derived in this limit if nonlocal effects like redeposition of sputtered material are neglected. We find the EOM not just in the high energy regime in which there is substantial sputtering, but also in the low energy regime in which the ion energy is below the sputtering threshold and consequently no sputtering occurs. In addition, we derive the EOM for ion energies just above the sputter yield threshold. For brevity, we will call this the intermediate energy regime.

In simulations carried out in the low energy regime, we find disordered arrays of nanoscale mounds (nanodots) that coarsen in time. Disordered arrays of nanodots also form in the high energy regime, but no coarsening occurs close to the threshold angle. Typically, a pattern with a high degree of order forms only if there is a narrow band of linearly unstable wavelengths [31], and this is the case in the high and low energy regimes. Surprisingly, however, our simulations show that in the intermediate energy regime, highly ordered hexagonal arrays of nanodots or nanoholes can emerge as the sample is bombarded, even though there is a broad band of unstable wavelengths. This finding might prove to be useful in applications in which patterns with a high degree of order are desirable or essential.

The behavior in the low and intermediate energy regimes is strongly influenced by the presence of a term in the EOM that is approximately proportional to the Gaussian curvature of the surface. This term has important effects on the dynamics but has invariably been neglected even though it is of the same order as other terms that are typically included in the EOM.

This paper is organized as follows. In Sec. II, we derive the equations governing the surface dynamics in the three regimes we have discussed and see that all three are special cases of a more general EOM. Various special cases of this general EOM are discussed in Sec. III, and it is recast in dimensionless form. We also show that certain special cases of this EOM are variational, i.e., the dynamics tends to minimize an effective free energy. This yields important insights into the dynamics. Simulations of the behavior in the low and intermediate regimes are carried out in Sec. IV. (The EOM that applies in the high-energy regime is already well understood.) We close the paper with a discussion of our results in Sec. V.

II. EQUATIONS OF MOTION

Consider a solid elemental material that is bombarded with a broad beam of noble gas ions with angle of incidence θ. The material may be amorphous or crystalline. However, if the material is initially crystalline, we assume that a layer at the surface of the solid is amorphized by the ion bombardment. We will make the customary assumption that the effect of ion implantation is negligible [30]. We will also take nonlocal effects to be negligible. Examples of effects of this kind include redeposition of sputtered material and sputtering by reflected ions. In past theoretical work, nonlocal effects have typically been neglected without comment.

We take the sample surface to be nominally flat before the irradiation begins. The unit vector $\hat{z}$ will be chosen to be normal to the macroscopic surface and to point away from the solid. The sample is rotated about the z axis with constant angular velocity ω. We will find it convenient to work in a corotating frame of reference with coordinates x, y, and z in which the sample is stationary. ω will be taken to be large enough that the effect of the ion bombardment is to an excellent approximation the same as if the sample were bombarded from all azimuthal angles ϕ simultaneously.

For polar angles of incidence θ less than the critical value θ_c, the solid surface is stable and it remains flat as the irradiation proceeds. Conversely, for $\theta > \theta_c$, the surface is unstable and a nanoscale pattern develops as time passes. Note that θ_c will, in general, depend on the ion energy E.

The goal of this section is to find the EOM for the surface for an angle of incidence θ just above the threshold value θ_c. This will be accomplished by carrying out systematic expansions in the small parameter $\epsilon \equiv (\theta - \theta_c)^{1/2}$. The three cases of high, low, and intermediate energies E will be considered in turn.

Let $h(x, y, t)$ be the height of the solid surface above the point (x, y) in the $x - y$ plane at time t. The partial derivative of h with respect to x will be denoted by h_x, and h_y and h_t are defined analogously. We will evaluate $h_t(0, 0, t)$, the time rate of change of h at $x = y = 0$. Because the point $x = y = 0$ can be placed at an arbitrary location, this will yield the EOM for the surface.

A. High-energy regime

Suppose that only ions with azimuthal angles of incidence between $-d\phi/2$ and $d\phi/2$ were incident on the surface of the solid. $h_t(0,0,t)$ depends on the polar angle of incidence θ. It also depends in principle on the shape of the entire surface or, equivalently, on all of the spatial derivatives of $h(x,y,t)$ evaluated at $x=y=0$. We will write

$$h_t = \frac{1}{2\pi} f(\theta; h_x, h_y, h_{xx}, h_{xy}, h_{yy}, h_{xxx}, h_{xxy}, h_{xyy}, h_{yyy}, h_{xxxx}, \dots) d\phi. \tag{1}$$

The partial derivatives of h that appear in Eq. (1) are all to be evaluated at $x=y=0$ and time t. The factor of $1/2\pi$ was inserted on the right-hand side of Eq. (1) merely because this will make our final result neater.

The function f includes the effects of sputtering and MR. It also includes either the effect of thermally activated surface diffusion or ion-induced viscous flow near the surface of the solid, depending on which of these two processes is active for the given ion energy and sample temperature.

In writing Eq. (1), we have assumed that inertial effects are negligible. This is completely reasonable, since even if there is ion-induced viscous flow near the surface of the solid, the viscosity is so high that the flow is in the Stokes regime. In addition, because the EOM must be invariant under the transformation $h \to h + \text{const}$, the function f cannot depend on h itself, although it certainly does depend on the spatial derivatives of h.

Let the coordinate axes obtained by rotating the x, y, and z axes through an angle ϕ about the z axis be denoted by x', y', and z'. When ions with all azimuthal angles of incidence ϕ impinge on the solid, Eq. (1) is replaced by

$$h_t = \frac{1}{2\pi}\int_0^{2\pi} f(\theta; h_{x'}, h_{y'}, h_{x'x'}, h_{x'y'}, h_{y'y'}, h_{x'x'x'}, \dots) d\phi. \tag{2}$$

Because

$$x' = x\cos\phi + y\sin\phi, \tag{3}$$

$$y' = -x\sin\phi + y\cos\phi, \tag{4}$$

and

$$z' = z, \tag{5}$$

the integrand on the right-hand side of Eq. (2) has an implicit dependence on ϕ and cannot simply be factored out from under the integral.

Although Eq. (2) gives h_t and so completely specifies the dynamics of the surface, it is an exceedingly complicated integrodifferential equation. In addition, we only have limited knowledge of the nature of the function f. Fortunately, Eq. (2) becomes much simpler when $\epsilon \equiv (\theta - \theta_c)^{1/2}$ is small and positive. Let $v_0 = -f(\theta; 0, 0, \dots)$ be the rate the surface recedes if it is perfectly planar, and set $h(x,y,t) = -v_0 t + u(x,y,t)$. We seek solutions to Eq. (2) of the form

$$u(x,y,t) = \epsilon^2 U(X,Y,T), \tag{6}$$

where

$$X \equiv \epsilon x, \quad Y \equiv \epsilon y, \quad \text{and} \quad T \equiv \epsilon^4 t. \tag{7}$$

X, Y, and T are the so-called slow variables and x, y, and t are the corresponding fast variables. Heuristically speaking, Eq. (6) says that close to the critical angle θ_c, the amplitude of the surface disturbance is small and it varies slowly in space and time. An *a posteriori* justification for adopting the scaling given by Eqs. (6) and (7) will be obtained once we have arrived at an EOM that is well-behaved in the $\epsilon \to 0$ limit.

We now insert Eq. (6) into $f(\theta; u_x, u_y, u_{xx}, u_{xy}, u_{yy}, \dots)$, expand in powers of ϵ, and retain terms up to order ϵ^6. Such an expansion is possible because we are neglecting nonlocal effects [32]. Terms that are not invariant under the transformation $y \to -y$ must have coefficients equal to zero and are discarded. So we can write the result of this expansion succinctly, we define

$$f_0(\theta) \equiv f(\theta; 0, 0, \dots), \tag{8}$$

$$f_1(\theta) \equiv \frac{\partial}{\partial u_x} f(\theta; u_x, 0, 0, \dots)\Big|_{u_x=0}, \tag{9}$$

$$f_2(\theta) \equiv \frac{\partial}{\partial u_y} f(\theta; 0, u_y, 0, 0, \dots)\Big|_{u_y=0}, \tag{10}$$

$$f_3(\theta) \equiv \frac{\partial}{\partial u_{xx}} f(x, y, \theta; 0, 0, u_{xx}, 0, 0, \dots)\Big|_{u_{xx}=0}, \tag{11}$$

and so on. Similarly, for positive integers n and m, $f_{n,m}(\theta)$ will denote the partial derivative of $f(\theta; u_x, u_y, u_{xx}, u_{xy}, \dots)$ with respect to the nth and mth arguments that appear after the semicolon, evaluated for all the arguments after the semicolon set equal to zero. For example,

$$f_{1,3}(\theta) \equiv \frac{\partial}{\partial u_x}\frac{\partial}{\partial u_{xx}} f(\theta; u_x, 0, u_{xx}, 0, 0, \dots)\Big|_{u_x=u_{xx}=0}. \tag{12}$$

We obtain

$$\begin{aligned} f(\theta; u_x, u_y, u_{xx}, u_{xy}, u_{yy}, \dots) &= f_0 + \epsilon^3 f_1 U_X + \epsilon^4 f_3 U_{XX} + \epsilon^4 f_5 U_{YY} + \epsilon^5 f_6 U_{XXX} \\ &\quad + \epsilon^5 f_8 U_{XYY} + \epsilon^6 f_{10} U_{XXXX} + \epsilon^6 f_{12} U_{XXYY} \\ &\quad + \epsilon^6 f_{14} U_{YYYY} + \tfrac{1}{2}\epsilon^6 f_{1,1} U_X^2 + \tfrac{1}{2}\epsilon^6 f_{2,2} U_Y^2. \end{aligned} \tag{13}$$

All of the spatial derivatives of U that appear on the right-hand side of Eq. (13) are evaluated at $X=Y=0$. Using the fact that $v_0 = -f_0$, we may rewrite Eq. (2) as

$$\begin{aligned} \epsilon^6 U_T = \frac{1}{2\pi}\int_0^{2\pi} d\phi \Big(&\epsilon^3 f_1 U_{X'} + \epsilon^4 f_3 U_{X'X'} + \epsilon^4 f_5 U_{Y'Y'} \\ &+ \epsilon^5 f_6 U_{X'X'X'} + \epsilon^5 f_8 U_{X'Y'Y'} + \epsilon^6 f_{10} U_{X'X'X'X'} \\ &+ \epsilon^6 f_{12} U_{X'X'Y'Y'} + \epsilon^6 f_{14} U_{Y'Y'Y'Y'} + \frac{1}{2}\epsilon^6 f_{1,1} U_{X'}^2 \\ &+ \frac{1}{2}\epsilon^6 f_{2,2} U_{Y'}^2 \Big), \end{aligned} \tag{14}$$

where $X' \equiv \epsilon x'$ and $Y' \equiv \epsilon y'$. Equation (14) is valid to sixth order in ϵ.

We will next do some preparatory work that will allow us to efficiently evaluate the integrals over azimuthal angles ϕ that appear in Eq. (14). These methods will also be used in the next subsection.

From Eqs. (3) and (4), we have

$$\partial_{X'} = (\cos\phi)\partial_X + (\sin\phi)\partial_Y \tag{15}$$

and

$$\partial_{Y'} = -(\sin\phi)\partial_X + (\cos\phi)\partial_Y. \tag{16}$$

If we simply inserted these results into the right-hand side of Eq. (14), we would be faced with computing integrals of products of up to four sines and/or cosines. Instead, we let $Z \equiv X + iY$ so that $Z^* = X - iY$. We immediately find that

$$\partial_Z = \tfrac{1}{2}(\partial_X - i\partial_Y) \tag{17}$$

and hence

$$\partial_{Z^*} = \tfrac{1}{2}(\partial_X + i\partial_Y). \tag{18}$$

Writing $\cos\phi$ and $\sin\phi$ as linear combinations of $e^{i\phi}$ and $e^{-i\phi}$ in Eqs. (15) and (16), we readily obtain

$$\partial_{X'} = e^{i\phi}\partial_Z + e^{-i\phi}\partial_{Z^*} \tag{19}$$

and

$$\partial_{Y'} = i(e^{i\phi}\partial_Z - e^{-i\phi}\partial_{Z^*}). \tag{20}$$

When we insert these expressions for $\partial_{X'}$ and $\partial_{Y'}$ into the right-hand side of Eq. (14), we only have to compute integrals of complex exponentials. For example,

$$\begin{aligned}
&\frac{1}{2\pi}\int_0^{2\pi} U_{X'X'} d\phi \\
&= \frac{1}{2\pi}\int_0^{2\pi} (e^{i\phi}\partial_Z + e^{-i\phi}\partial_{Z^*})^2 U d\phi \\
&= \frac{1}{2\pi}\int_0^{2\pi} (e^{2i\phi}U_{ZZ} + 2U_{ZZ^*} + e^{-2i\phi}U_{Z^*Z^*}) d\phi \\
&= 2U_{ZZ^*} = \frac{1}{2}\nabla_X^2 U,
\end{aligned} \tag{21}$$

where Eqs. (17) and (18) have been used in the final step and $\nabla_X^2 \equiv \partial_X^2 + \partial_Y^2$. Once all of the integrals on the right-hand side of Eq. (14) have been evaluated, we are left with

$$\epsilon^6 U_T = -\mathcal{A}\epsilon^4\nabla_X^2 U - \mathcal{B}\epsilon^6\nabla_X^2\nabla_X^2 U + \lambda\epsilon^6(\nabla_X U)^2, \tag{22}$$

where $\boldsymbol{\nabla}_X \equiv \partial_X\hat{\boldsymbol{x}} + \partial_Y\hat{\boldsymbol{y}}$,

$$\mathcal{A} \equiv -\tfrac{1}{2}(f_3 + f_5), \tag{23}$$

$$\mathcal{B} \equiv -\tfrac{3}{8}(f_{10} - f_{12} + f_{14}), \tag{24}$$

and

$$\lambda \equiv \tfrac{1}{4}(f_{1,1} + f_{2,2}). \tag{25}$$

As the angle of incidence θ passes through the critical value θ_c, an instability sets in and the coefficient $\mathcal{A}$ must change sign from negative to positive. Thus, close to the transition, $\mathcal{A} \cong \mathcal{A}_1(\theta - \theta_c)$, where $\mathcal{A}_1$ is a positive constant that does not depend on θ. Just above the transition, $\mathcal{A} \cong \mathcal{A}_1\epsilon^2$. The EOM (22) is therefore

$$U_T = -\mathcal{A}_1\nabla_X^2 U - \mathcal{B}\nabla_X^2\nabla_X^2 U + \lambda(\nabla_X U)^2 \tag{26}$$

for θ just above θ_c. Notice that ϵ does not appear in Eq. (26). Thus, the scaling we posited in Eqs. (6) and (7) leads to a well-behaved EOM in the small ϵ limit.

In terms of the original variables, Eq. (26) is

$$u_t = -\mathcal{A}\nabla^2 u - \mathcal{B}\nabla^2\nabla^2 u + \lambda(\nabla u)^2. \tag{27}$$

Equation (27) is the isotropic two-dimensional KS equation. Note that we must have $\mathcal{B} > 0$ for the solutions to Eq. (27) to be well-defined. For $\theta > \theta_c$, the constant $\mathcal{A}$ is positive and a flat initial surface is unstable. The surface width $\langle w\rangle$ grows exponentially at early times. At longer times, $\langle w\rangle$ tends to a constant and the surface exhibits spatiotemporal chaos.

The term proportional to $\nabla^2 u$ in Eq. (27) comes from curvature-dependent sputtering and MR. The term $-\mathcal{B}\nabla^2\nabla^2 u$, on the other hand, describes the effect of thermally activated surface diffusion or ion-induced viscous flow near the surface of the solid. The origin of the term $\lambda(\nabla u)^2$ is the slope dependence of the sputter yield.

B. Low-energy regime

We now turn our attention to the case in which the energy per incident ion E is below the sputtering threshold and sputtering is therefore negligible. Because ion implantation can be neglected, the mass of the solid is conserved and the continuity equation applies. Let $\boldsymbol{J}$ be the total surface current and set $u = h$. The continuity equation is then

$$u_t = -\Omega\nabla\cdot\boldsymbol{J}, \tag{28}$$

where Ω is the atomic volume.

Suppose that only ions with azimuthal angles of incidence between $-d\phi/2$ and $d\phi/2$ were incident on the surface of the solid. The resulting surface current, which we will denote by $\frac{1}{2\pi}\boldsymbol{j}(0)d\phi$, depends on the polar angle of incidence θ. It also depends, in principle, on the shape of the entire surface or, equivalently, on all of the spatial derivatives of $u(x, y, t)$ evaluated at $x = y = 0$. We will write

$$j_i(0) = j_i(\theta; u_x, u_y, u_{xx}, u_{xy}, u_{yy}, u_{xxx}, \ldots) \tag{29}$$

for $i = x$ and y. Similarly, we let $\frac{1}{2\pi}\boldsymbol{j}(\phi)d\phi$ denote the surface current if only ions with azimuthal angles of incidence between $\phi - d\phi/2$ and $\phi + d\phi/2$ are incident on the surface of the solid. In analogy with Eq. (29), we have

$$j_i(\phi) = j_i(\theta; u_{x'}, u_{y'}, u_{x'x'}, u_{x'y'}, u_{y'y'}, u_{x'x'x'}, \ldots) \tag{30}$$

for $i = x'$ and y'.

When ions with all azimuthal angles of incidence impinge on the solid surface, the surface current is

$$\boldsymbol{J} = \frac{1}{2\pi}\int_0^{2\pi} \boldsymbol{j}(\phi)d\phi. \tag{31}$$

The continuity equation (28) becomes

$$\begin{aligned}
u_t &= -\frac{\Omega}{2\pi}\int_0^{2\pi} [\partial_{x'}j_{x'}(\phi) + \partial_{y'}j_{y'}(\phi)]d\phi \\
&= -\frac{\Omega}{2\pi}\int_0^{2\pi} [\partial_{x'}j_{x'}(\theta; u_{x'}, u_{y'}, u_{x'x'}, \ldots) \\
&\quad + \partial_{y'}j_{y'}(\theta; u_{x'}, u_{y'}, u_{x'x'}, \ldots)]d\phi.
\end{aligned} \tag{32}$$

The partial derivatives of u that appear in Eq. (32) are all to be evaluated at $x = y = 0$.

We seek solutions to Eq. (32) of the form

$$u(x,y,t)=U(X,Y,T), \tag{33}$$

where

$$X\equiv\epsilon x,\quad Y\equiv\epsilon y,\quad \text{and}\quad T\equiv\epsilon^4 t. \tag{34}$$

Once again, X, Y and T are the slow variables and x, y and t are the corresponding fast variables. Heuristically speaking, Eq. (33) says that close to the critical angle θ_c, the surface disturbance varies slowly in space and time. An *a posteriori* justification for adopting the scaling given by Eqs. (33) and (34) will again be obtained when we have arrived at an EOM that is well-behaved in the $\epsilon\to 0$ limit. Note that Eq. (33) differs from Eq. (6): different scaling ansatzes are needed in the high- and low-energy regimes, as in the case in which the sample is not rotating [33,34].

We now insert Eq. (33) into Eq. (32) and expand in powers of ϵ. We retain terms up to order ϵ^4. Once that has been done, the integrals over the azimuthal angle must be evaluated. The calculation is lengthy and arduous, but it is simplified by using Eqs. (19) and (20), as before. The partial derivatives $j_{x,n}(\theta)$ and $j_{y,n}(\theta)$ are defined in complete analogy with the definition of $f_n(\theta)$. In addition, for positive integers n and m, $j_{x,n,m}(\theta)$ will denote the partial derivative of $j_x(\theta; u_x, u_y, u_{xx}, u_{xy},\ldots)$ with respect to the nth and mth arguments that appear after the semicolon, evaluated for all the arguments after the semicolon set equal to zero. Naturally, $j_{y,n,m}(\theta)$ is defined in an exactly parallel fashion. The end result is the EOM

$$\begin{aligned}\epsilon^4 U_T = & -A\epsilon^2\nabla_X^2 U - B\epsilon^4\nabla_X^2\nabla_X^2 U\\ & +\beta\epsilon^4\left(U_{XX}U_{YY}-U_{XY}^2\right)+r\epsilon^4\nabla_X^2(\nabla_X U)^2\\ & +\nu\epsilon^4\nabla_X\cdot[(\nabla_X U)^2\nabla_X U],\end{aligned} \tag{35}$$

where

$$A\equiv\tfrac{1}{2}\Omega(j_{x,1}+j_{y,2}), \tag{36}$$

$$B\equiv\tfrac{3}{8}\Omega(j_{x,6}-j_{x,8}+j_{y,9}-j_{y,7}), \tag{37}$$

$$\beta=-\tfrac{1}{4}\Omega(j_{x,1,3}+3j_{x,1,5}-j_{x,2,4}+j_{y,2,5}+3j_{y,2,3}-j_{y,1,4}), \tag{38}$$

$$r=-\tfrac{1}{16}\Omega(3j_{x,1,3}+j_{x,1,5}+j_{x,2,4}+3j_{y,2,5}+j_{y,2,3}+j_{y,1,4}), \tag{39}$$

and

$$\nu=-\tfrac{1}{16}\Omega(j_{x,1,1,1}+j_{x,1,2,2}+j_{y,2,2,2}+j_{y,1,1,2}). \tag{40}$$

Arguing just as we did in Sec. II A for the high-energy regime, we find that $A\cong A_1\epsilon^2$ for θ just above θ_c. Here A_1 is a positive constant that does not depend on θ. The EOM (35) is therefore

$$\begin{aligned}U_T = & -A_1\nabla_X^2 U - B\nabla_X^2\nabla_X^2 U\\ & +\beta\left(U_{XX}U_{YY}-U_{XY}^2\right)+r\nabla_X^2(\nabla_X U)^2\\ & +\nu\nabla_X\cdot[(\nabla_X U)^2\nabla_X U],\end{aligned} \tag{41}$$

for θ just above θ_c. Notice that ϵ does not appear in Eq. (41). Thus, the scaling we posited in Eqs. (33) and (34) leads to a well-behaved EOM in the small ϵ limit.

In terms of the original variables, Eq. (41) is

$$\begin{aligned}u_t = & -A\nabla^2 u - B\nabla^2\nabla^2 u+\beta\left(u_{xx}u_{yy}-u_{xy}^2\right)+r\nabla^2(\nabla u)^2\\ & +\nu\nabla\cdot[(\nabla u)^2\nabla u].\end{aligned} \tag{42}$$

Once again, we must have $B>0$ for the solutions to Eq. (42) to be well-defined. In addition, the constant ν must be positive; if it is negative or zero, the surface slope will grow without bound.

It is not immediately apparent that Eq. (42) conserves mass. However, using the identity

$$u_{xx}u_{yy}-u_{xy}^2=\tfrac{1}{2}\nabla\cdot[(\nabla^2 u)\nabla u]-\tfrac{1}{4}\nabla^2(\nabla u)^2, \tag{43}$$

we see that Eq. (42) may be written in the form of a continuity equation

$$u_t=-\Omega\nabla\cdot\bar{\boldsymbol{J}}, \tag{44}$$

where the approximate surface current $\bar{\boldsymbol{J}}$ is given by

$$\begin{aligned}\Omega\bar{\boldsymbol{J}} = & A\nabla u+B\nabla\nabla^2 u+\left(\tfrac{1}{4}\beta-r\right)\nabla(\nabla u)^2\\ & -\tfrac{1}{2}\beta(\nabla^2 u)\nabla u-\nu(\nabla u)^2\nabla u.\end{aligned} \tag{45}$$

Mass is therefore conserved. Equation (43) also makes it clear that Eq. (42) is invariant under rotations about the z axis, as it must be.

In the low-energy regime, there is no sputtering, and so only MR contributes to the term $-A\nabla^2 u$ in Eq. (42). As in the high-energy regime, the term $-B\nabla^2\nabla^2 u$ describes the effect of thermally activated surface diffusion or ion-induced viscous flow near the surface of the solid. The term $r\nabla^2(\nabla u)^2$, on the other hand, is the conserved Kuramoto-Sivashinsky (CKS) nonlinearity. Although this term was first encountered in molecular beam epitaxy [35,36], it plays a role in ion-induced pattern formation even when a surface layer of the target material is amorphized by the ion bombardment [37–39]. The CKS nonlinearity tends to produce coarsening of the surface patterns, i.e., the characteristic lateral and vertical length scales increase with time [37–40]. Because coarsening is commonly observed when solid surfaces are bombarded with broad ion beams, it is believed that the CKS nonlinearity must, in general, be included in the EOM.

A term similar to the term $\nu\nabla\cdot[(\nabla u)^2\nabla u]$ in Eq. (42) appears in the EOM that describes the mounding instability that can occur during molecular beam epitaxy. In that context, the term results from the Ehrlich-Schwoebel (ES) effect, is anisotropic, and can lead to the formation of a faceted surface [36]. In our problem, the term $\nu\nabla\cdot[(\nabla u)^2\nabla u]$ is isotropic and it appears in the EOM (42) as a result of the slope dependence of the surface current produced by MR.

It remains to discuss the term $\beta(u_{xx}u_{yy}-u_{xy}^2)$ that appears in Eq. (42). The Gaussian curvature K is given by

$$K=\frac{u_{xx}u_{yy}-u_{xy}^2}{\left(1+u_x^2+u_y^2\right)^2}. \tag{46}$$

To fourth order in ϵ, the factor of $u_{xx}u_{yy}-u_{xy}^2$ in Eq. (42) can be replaced by K. There is therefore a contribution to the surface velocity u_t that is approximately proportional to the Gaussian curvature. The effects of a term proportional to K have not previously been included in simulations of the dynamics of a solid surface subjected to ion bombardment.

However, it is of the same order in ϵ as the other terms in the EOM (42) and so it must be retained for the sake of consistency.

In their derivation of an EOM that models the deposition of amorphous thin films, Raible *et al.* at first included a Gaussian curvature term (GCT) [41]. At this stage of their derivation, their EOM was Eq. (42) with ν set to zero. However, Raible and coworkers then argued that the GCT is negligible in the case of thin film deposition and discarded it.

The effects of the GCT on the surface dynamics will be explored in detail in this paper. As we shall see, it can have an important influence on the dynamics and cannot be omitted from the EOM, at least in the case of ion bombardment of a solid.

C. Intermediate-energy regime

We now turn to the intermediate energy regime, i.e., to ion energies just above the sputtering threshold. In this regime, we divide the contributions to the surface velocity h_t into two parts: one from surface currents and the other from sputtering. We choose the ion energy to be above the sputtering threshold but close enough to it that the contribution from sputtering is of order ϵ^2. Thus, in analogy with Eqs. (2) and (32), we have

$$\begin{aligned} h_t = & -\frac{\Omega}{2\pi}\int_0^{2\pi}[\partial_{x'}j_{x'}(\theta;h_{x'},h_{y'},h_{x'x'},\dots) \\ & +\partial_{y'}j_{y'}(\theta;h_{x'},h_{y'},h_{x'x'},\dots)]d\phi \\ & +\frac{1}{2\pi}\epsilon^2\int_0^{2\pi} f(\theta;h_{x'},h_{y'},h_{x'x'}, \\ & h_{x'y'},h_{y'y'},h_{x'x'x'},\dots)d\phi, \end{aligned} \tag{47}$$

where the $O(\epsilon^2)$ magnitude of the contribution to h_t from sputtering has been explicitly displayed.

We once again set $h(x,y,t) = -v_0t + u(x,y,t)$ and seek solutions to Eq. (47) of the form given by Eqs. (33) and (34). We retain terms up to order ϵ^4. The required expansions for the two terms on the right-hand side of Eq. (47) were carried out in the preceding two subsections, although the expansion for the second term on the right-hand side of Eq. (47) must be modified because there is a prefactor of ϵ^2 on the right-hand side of Eq. (6) but not on the right-hand side of Eq. (33). We obtain

$$\begin{aligned} U_T = & -A_1\nabla_X^2U - B\nabla_X^2\nabla_X^2U + \lambda(\nabla_XU)^2 \\ & +\beta\big(U_{XX}U_{YY}-U_{XY}^2\big) + r\nabla_X^2(\nabla_XU)^2 \\ & +\nu\nabla_X\cdot[(\nabla_XU)^2\nabla_XU]. \end{aligned} \tag{48}$$

Because ϵ does not appear in Eq. (48), this equation has a well-defined $\epsilon \to 0$ limit. In terms of the original variables, Eq. (48) is

$$\begin{aligned} u_t = & -A\nabla^2u - B\nabla^2\nabla^2u + \lambda(\nabla u)^2 + \beta\big(u_{xx}u_{yy}-u_{xy}^2\big) \\ & + r\nabla^2(\nabla u)^2 + \nu\nabla\cdot[(\nabla u)^2\nabla u]. \end{aligned} \tag{49}$$

It is perhaps not surprising that all of the nonlinear terms on the right-hand side of the high-energy EOM (27) and the low-energy EOM (42) appear on the right-hand side of Eq. (49), the EOM that applies in the intermediate-energy regime.

If $\beta = r = \lambda = 0$, Eq. (49) is invariant under the transformation $u \to -u$. If, on the other hand, β, r, or λ is nonzero, then the $u \to -u$ symmetry is broken. Since there is vacuum above the surface and solid below, there is no reason that such a symmetry should exist.

A term proportional to K appears in the EOM in the intermediate-energy regime, just as in the low-energy regime. In the intermediate-energy regime, however, the term proportional to K could contain a contribution that comes from sputtering. Monte Carlo simulations have shown that a term proportional to K makes an non-negligible contribution to the yield in nanoparticle sputtering, albeit for ion energies well in excess of the sputtering threshold [42]. This again suggests that the term proportional to K cannot simply be omitted when studying the dynamics of a surface that is bombarded with a broad ion beam.

III. PRELIMINARY DISCUSSION OF THE SURFACE DYNAMICS

We have seen that the EOM is Eq. (49) in the high-, low-, and intermediate-energy regimes. In the high-energy regime, $\beta = r = \nu = 0$ and the EOM is the isotropic KS equation. This equation has been studied extensively, and so this regime will not be discussed further. In the low-energy regime, $\lambda = 0$ and the mass of the solid is conserved. Finally, in the intermediate-energy regime, λ, β, r, and ν could all be nonzero.

Various special cases of Eq. (49) with the coefficient of the Gaussian curvature term β equal to zero have already been studied. For $\beta = \nu = 0$, Eq. (49) reduces to the so-called extended KS equation. Solutions to this equation exhibit interrupted coarsening: the characteristic lateral and vertical length scales grow at first, but ultimately saturate [37,38,40,43]. For $\beta = r = 0$, on the other hand, Eq. (49) is a special case of a model that governs the faceting of growing, thermodynamically unstable crystal surfaces [44,45]. Finally, for $\beta = \lambda = 0$, Eq. (49) is a special case of a model that describes the epitaxial growth of a crystal [36]. In the second and third special cases just mentioned, the ES term is isotropic. In contrast, the ES term for the surface of a crystal is in general anisotropic.

The novel feature of Eq. (49) is the presence of the GCT, and so we will focus on the case in which β is nonzero in this paper. Because the GCT vanishes in one dimension, we will confine our discussion to the two-dimensional case in which u depends on both x and y. We introduce the dimensionless quantities $\tilde{x} \equiv (A/B)^{1/2}x$, $\tilde{y} \equiv (A/B)^{1/2}y$, $\tilde{t} \equiv A^2t/B$, $\tilde{u} \equiv \beta u/B$, $\tilde{\lambda} = B\lambda/(\beta A)$, $\tilde{r} \equiv r/\beta$, and $\tilde{\nu} = B\nu/\beta^2$. After dropping the tildes, Eq. (49) becomes

$$\begin{aligned} u_t = & -\nabla^2u - \nabla^2\nabla^2u + u_{xx}u_{yy} - u_{xy}^2 + \lambda(\nabla u)^2 + r\nabla^2(\nabla u)^2 \\ & + \nu\nabla\cdot[(\nabla u)^2\nabla u]. \end{aligned} \tag{50}$$

For $r = \nu = 0$, Eq. (50) is a special case of a partial differential equation that was employed as a model of combustion fronts and the solidification of a hypercooled melt in Ref. [46]. That particular special case of the model, however, was not studied in Ref. [46] or in subsequent work.

We wish to highlight the effects of the GCT in Eq. (50). Therefore, we will also consider the surface dynamics given by the EOM

$$u_t = -\nabla^2 u - \nabla^2\nabla^2 u + \lambda(\nabla u)^2 + r\nabla^2(\nabla u)^2 + \nu\boldsymbol{\nabla}\cdot[(\nabla u)^2\boldsymbol{\nabla} u], \tag{51}$$

i.e., Eq. (50) with the GCT omitted. Comparisons will be made between the behavior predicted by Eqs. (50) and (51) with the same values of the parameters λ, r, and ν.

To understand the effects of the ES term $\nu\boldsymbol{\nabla}\cdot[(\nabla u)^2\boldsymbol{\nabla} u]$ that appears in both Eqs. (50) and (51), let us consider the behavior of solutions to Eq. (51) with $\lambda = r = 0$ on the domain in which $0 \leqslant x \leqslant L$ and $0 \leqslant y \leqslant L$ and apply periodic boundary conditions. We introduce the effective free energy

$$F_{\text{ES}} \equiv \int_0^L \int_0^L \left[f(u_x, u_y) + \frac{1}{2}(\nabla^2 u)^2\right] dxdy, \tag{52}$$

where

$$f(u_x, u_y) \equiv -\tfrac{1}{2}(\nabla u)^2 + \tfrac{1}{4}\nu(\nabla u)^4 \tag{53}$$

will be referred to as the effective potential. For $\lambda = r = 0$, Eq. (51) can be written

$$u_t = -\frac{\delta F_{\text{ES}}}{\delta u}, \tag{54}$$

where $\delta F_{\text{ES}}/\delta u$ denotes the variational derivative of F_{ES} with respect to the surface height u. Equation (54) implies that $dF_{\text{ES}}/dt \leqslant 0$, i.e., the effective free energy can never increase. The dynamics therefore tends to minimize the value of F_{ES}. The effective potential f is minimized for $|\nabla u| = \nu^{-1/2}$ and, as a result, the surface will tend toward a state in which most of the surface has a gradient of magnitude close to $\nu^{-1/2}$. The term $\nu\boldsymbol{\nabla}\cdot[(\nabla u)^2\boldsymbol{\nabla} u]$ in Eqs. (50) and (51) therefore tends to prevent the development of large surface slopes. Spatial variations of the direction of ∇u have an energy cost because of the second term in the integrand in Eq. (52).

To illustrate the conclusions of the previous paragraph, we carried out a simulation of Eq. (51) with $\lambda = r = 0$ and $\nu = 1$ starting from a low-amplitude spatial white noise initial condition. (Our simulation method is described in Sec. IV.) The surface at time $t = 1000$ is shown in Fig. 1(a). The heat map of $|\boldsymbol{\nabla} u|$ in Fig. 1(b) demonstrates that by time $t = 1000$, $|\boldsymbol{\nabla} u|$ is close to the predicted value $\nu^{-1/2} = 1$ over much of the surface, but there are intervening, nearly straight regions in which the surface slope is near zero. The distribution of surface gradients given in Fig. 1(c) shows more clearly that, by this time, $|\boldsymbol{\nabla} u|$ is close to one at most points on the surface. Finally, Fig. 1(d) shows that the probability distribution of $|\boldsymbol{\nabla} u|$ has a peak that moves toward the expected value of 1 as time passes.

To gain insight into the effect of the GCT, consider Eq. (50) with all of the terms on the right-hand side omitted except the GCT. Thus, we will study the partial differential equation

$$u_t = u_{xx}u_{yy} - u_{xy}^2. \tag{55}$$

To fourth order in ϵ, this may be replaced by

$$u_t = \frac{u_{xx}u_{yy} - u_{xy}^2}{\left(1 + u_x^2 + u_y^2\right)^{3/2}}. \tag{56}$$

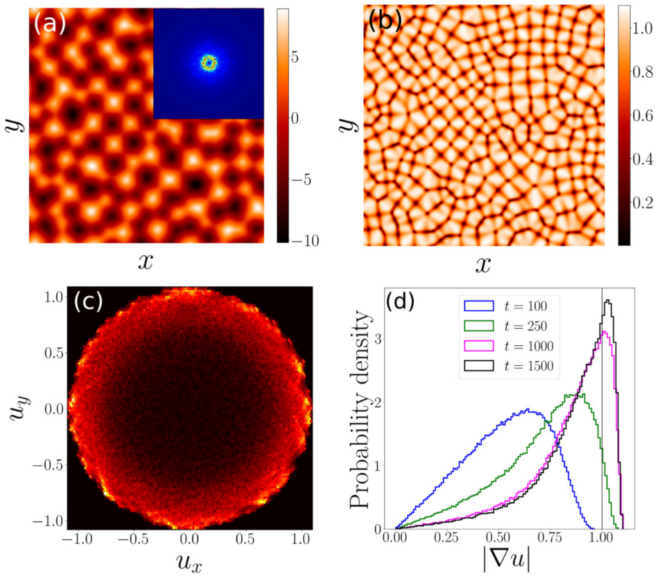

FIG. 1. Results from a simulation of Eq. (51) with $\lambda = r = 0$ and $\nu = 1$ starting with a low-amplitude spatial white noise initial condition. The surface height at time $t = 1000$ is shown in (a), along with its power spectral density in the inset. (b) shows the magnitude of the gradient of the surface shown in (a). In (c), the 2D gradient distribution is plotted for the surface shown in (a). (d) shows the probability distribution of the gradient's magnitude at three different times: $t = 100$ in blue, $t = 250$ in green, $t = 1000$ in magenta, and $t = 1500$ in black. The simulation parameters were $N = 512$ and $L = 30\pi$.

The normal velocity of the surface is $v_n = (1 + u_x^2 + u_y^2)^{-1/2}u_t$. Making use of this formula and of Eq. (46), Eq. (56) becomes

$$v_n = K. \tag{57}$$

The surface dynamics given by this equation is known as motion by Gaussian curvature. Remarkably, Eq. (57) can be written in variational form [47]. We introduce the effective free energy for motion by Gaussian curvature,

$$F_H = \int_S H dA, \tag{58}$$

where S is the surface of the solid, dA is an element of surface area, and H is the mean curvature of the surface. We adopt the sign convention that H is positive where the surface is concave, so that

$$H = \frac{\left(1 + u_y^2\right)u_{xx} - 2u_x u_y u_{xy} + \left(1 + u_x^2\right)u_{yy}}{2\left(1 + u_x^2 + u_y^2\right)^{3/2}}. \tag{59}$$

As shown in Ref. [47], Eq. (57) may be recast as

$$u_t = -\frac{\delta F_H}{\delta u}. \tag{60}$$

This means that the value of the effective free energy F_H can never increase, i.e., motion by Gaussian curvature tends to minimize the total mean curvature. By the Gauss-Bonnet theorem, Eq. (57) conserves mass, and so this minimization process occurs subject to the constraint that the total mass is conserved.

Although Eq. (57) has been studied in the past, the work done to date appears to have been entirely analytical and to have been restricted to the time evolution of smooth, convex surfaces [47–50]. Numerical integrations of Eq. (57) rapidly lead to pathological behavior and show that this work is largely academic. To see why this is so, suppose that u is small and work to second order in u. Equation (56) then reduces to Eq. (55). The surface $u(x, y, t) = -\frac{1}{2}Cx^2 \equiv u_0(x)$ with $C > 0$ is a steady-state solution to Eq. (55). If we perturb this solution to give $u(x, y, t) = u_0(x) + u_1(x, y, t)$ and linearize in the perturbation u_1, we obtain $u_{1,t} = -Cu_{1,yy}$. As a consequence, the amplitude of a Fourier mode with wave vector $\boldsymbol{k} = k_y\hat{\boldsymbol{y}}$ grows exponentially in time with the growth rate Ck_y^2. This growth rate diverges as the wavelength of the mode $2\pi/k_y$ tends to zero, which means that the continuum description of the surface breaks down. To remedy this problem, instead of continuing to study Eq. (55), we consider instead the partial differential equation

$$u_t = u_{xx}u_{yy} - u_{xy}^2 - \nabla^2\nabla^2 u. \tag{61}$$

This EOM does not break down at short wavelengths and simply incorporates another term that appears in Eq. (50).

Equation (61) is variational, as we now show. Inserting Eq. (59) into Eq. (58), using $dA = \sqrt{1 + u_x^2 + u_y^2}dxdy$, and retaining terms up to fourth order in ϵ, we obtain

$$F_H \cong -\int u_x u_y u_{xy} d^2x \equiv F_H', \tag{62}$$

where $d^2x \equiv dxdy$. F_H' is the free energy associated with Eq. (55), as is readily verified by computing the variational derivative $\delta F_H'/\delta u$ directly. The free energy for Eq. (61) is $F \equiv F_H' + F_D$, where

$$F_D \equiv \frac{1}{2}\int (\nabla^2 u)^2 d^2x. \tag{63}$$

To explore the time evolution described by Eq. (61), we compute the effective free energy F for the Gaussian surface profile

$$u(x, y) = \frac{V}{2\pi\sigma^2}e^{-(x^2+y^2)/2\sigma^2}. \tag{64}$$

Here $\sigma > 0$ is the width of the Gaussian and V is the volume beneath it. A straightforward calculation shows that for this variational trial function

$$F = \frac{V^2}{4\pi}\left(\frac{1}{\sigma^6} - \frac{V}{\pi\sigma^8}\right). \tag{65}$$

F is an increasing function of σ for σ less than the critical value $\sigma_c \equiv (4V/3\pi)^{1/2}$ and is a decreasing function for $\sigma > \sigma_c$. For $\sigma > \sigma_c$, therefore, σ will increase as time passes, i.e., the Gaussian will become broader and its height will decline to reduce the effective free energy. Conversely, the Gaussian will become narrower and higher as time passes for $\sigma < \sigma_c$. In fact, we expect that σ will tend to zero in this case, i.e., the surface protrusion will evolve into a singular spike.

The time evolution of a surface depression can be explored by replacing V by $-V$ in the trial function (64). The corresponding effective free energy

$$F = \frac{V^2}{4\pi^2}\left(\frac{1}{\sigma^6} + \frac{V}{\pi\sigma^8}\right) \tag{66}$$

is a decreasing function of σ. We conclude that a surface depression will become shallower and broader with the passage of time.

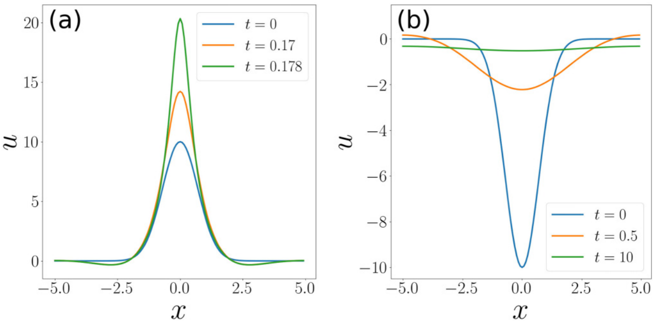

FIG. 2. $u(x, 0, t)$ versus x for two simulations of Eq. (61) at three different times. In (a), the initial condition was an upright Gaussian of height 10 and width $\sigma = 1$. Blue is time $t = 0$, orange is $t = 0.17$, and green is $t = 0.178$. In (b), the initial condition was an inverted Gaussian of depth 10 and width $\sigma = 1$. Blue is time $t = 0$, orange is $t = 0.5$, and green is $t = 10$. The simulation parameters were $L = 5$, $N = 128$, and $\Delta t = 0.0001$.

The results of a simulation of Eq. (61) with a Gaussian initial condition of the form (64) with width $\sigma = 1$ and height $V/2\pi = 10$ are shown in Fig. 2(a). The figure shows $u(x, 0, t)$ versus x for three different times. The chosen value of σ is smaller than $\sigma_c \cong 5.16$ and, as predicted, the surface protrusion becomes higher and narrower with time. A simulation for an inverted Gaussian initial condition with $\sigma = 1$ and $V/2\pi = -10$ yields a surface depression that becomes shallower and broader as time passes; see Fig. 2(b). This is again in accord with our prediction.

We next turn our attention to Eq. (50) when $\lambda = r = 0$ and ν is positive. This EOM is also variational, and it has the effective free energy $F_{\text{tot}} \equiv F_{\text{ES}} + F_H'$. If ν is sufficiently large in magnitude, we expect that runaway growth of spikes will be prevented by the presence of the term $\nu\nabla \cdot [(\nabla u)^2\boldsymbol{\nabla} u]$, for, as we have seen, the latter term tends to suppress the development of large surface slopes. This expectation is borne out by the simulations discussed in Sec. IV A.

IV. SIMULATIONS

For the simulations, the surface was approximated by a $N \times N$ grid of points evenly spaced on the spatial domain with $-L \leqslant x \leqslant L$ and $-L \leqslant y \leqslant L$. Periodic boundary conditions were employed. All of the simulations in this section were done with a low-amplitude spatial white noise initial condition. (The amplitude of the noise was chosen to be 10^{-3}.) The numerical integrations were carried out using fourth-order Runge-Kutta exponential time differencing (ETDRK4) [51,52]. In ETDRK4, the linear terms are evaluated exactly in Fourier space, and the nonlinear terms are approximated using finite differencing in real space. In particular, the KS and GCT terms were both evaluated only using finite differencing. The CKS and ES terms were evaluated using both finite differencing and a pseudospectral method. For example, the CKS term $r\nabla^2(\nabla u)^2$ was approximated by calculating $(\nabla u)^2$ in real space using finite differencing, but the the Laplacian

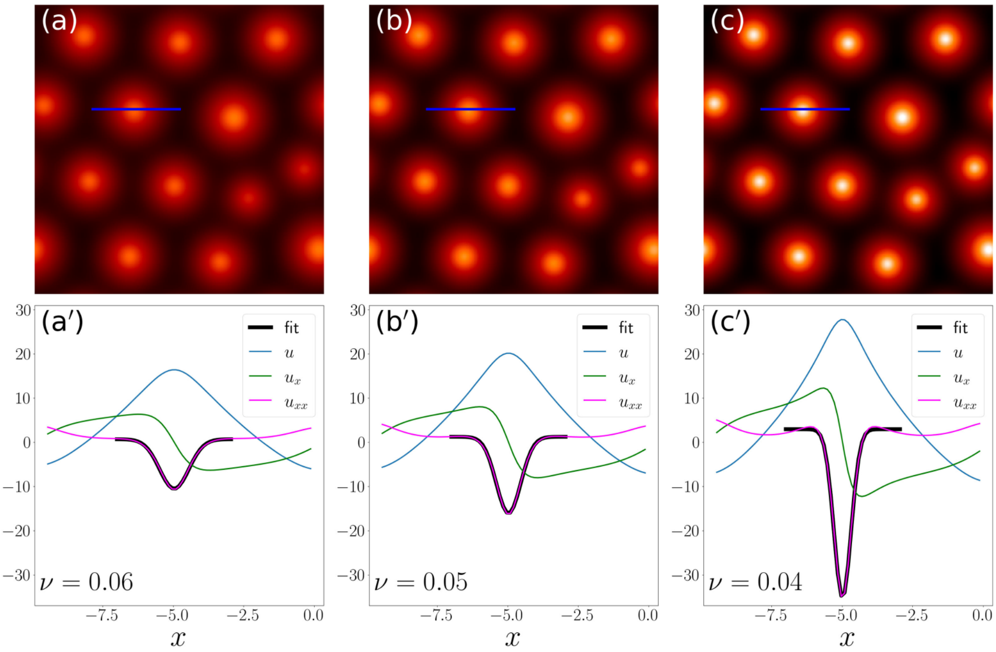

FIG. 3. Images taken from simulations of Eq. (50) at time $t = 2000$ with a low-amplitude noise initial condition and parameters $\lambda = r = 0$ and (a) $\nu = 0.06$, (b) $\nu = 0.05$, and (c) $\nu = 0.04$. High points are light and low points are dark. The blue horizontal lines indicate the directions of line scans along which data is shown in (a′), (b′), and (c′). The graphs (a′)–(c′) show the surface height u in blue, the slope u_x in green, the curvature u_{xx} in magenta, and the inverted Gaussian fits to the curvature in black. For these simulations, $N = 256$ and $L = 5\pi$.

of the result was then evaluated in Fourier space. Unless otherwise noted, the simulation parameters in the following results were $L = 30\pi$ and $N = 512$, and the time step was $\Delta t = 0.01$. We checked numerical accuracy by verifying that increasing N and decreasing Δt did not affect the results substantially.

In the simulation results, we often include plots of the power spectral density (PSD) as insets in plots of the surface height. The PSD was defined to be the square root of the modulus of the Fourier transform of the surface height. This definition yields more detail than if the PSD had been defined in the conventional way as the modulus of the Fourier transform squared. The region of k space shown in each PSD is the one in which $-2.5 \leqslant k_x \leqslant 2.5$ and $-2.5 \leqslant k_y \leqslant 2.5$.

A. The low-energy regime

In the low-energy regime, the EOM is Eq. (50) with $\lambda = 0$. The parameter r is an arbitrary real number. The value of ν, on the other hand, must be positive to prevent the formation of singularities, as we anticipated. To demonstrate this, we simulated Eq. (50) with $\lambda = r = 0$ and small, positive values of ν. Figure 3 shows surfaces obtained for (a) $\nu = 0.06$, (b) $\nu = 0.05$, and (c) $\nu = 0.04$ starting from a low-amplitude spatial white noise initial condition. Corresponding 1D line profiles of surface height u, slope u_x, and curvature u_{xx} of a representative spike from each are shown in Figs. 3(a′)–3(c′). These figures point to the development of progressively taller spikes with sharper tips as the value of ν is reduced. The curvature u_{xx} near the tip of the spike has an approximately Gaussian profile. Fitting (inverted) Gaussians to the data for u_{xx} shows that the depth of the Gaussian increases and its width decreases as ν approaches zero, as can be seen in Fig. 4. This provides additional numerical evidence that a singularity in the curvature develops in the limit that $\nu \to 0$. For values of ν smaller than 0.038, numerical blowup occurred for the choice of simulation parameters $N = 256$ and $L = 5\pi$.

Simulations of the version of Eq. (50) that applies in the low-energy regime all yield disordered arrays of nanodots that coarsen with time; however, the coarsening speed and mechanism depend on the value of the coefficient r of the CKS term. In Fig. 5, simulations of Eq. (50) with $\lambda = 0$ and $\nu = 0.1$ are shown with time progressing from left to right: on the left, $t = 50$; in the middle, $t = 150$; and on the

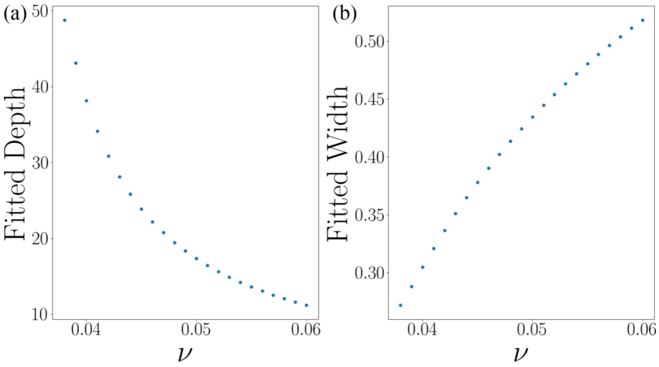

FIG. 4. Values of the (a) depth and (b) width of the Gaussian fits to the u_{xx} profile along a line passing through a spike for small values of ν. These results were obtained from simulations of Eq. (50) starting with a low-amplitude noise initial condition for the parameter values $\lambda = r = 0$, the same values used in Fig. 3. The data displayed are for time $t = 2000$. For these simulations, $N = 256$ and $L = 5\pi$.

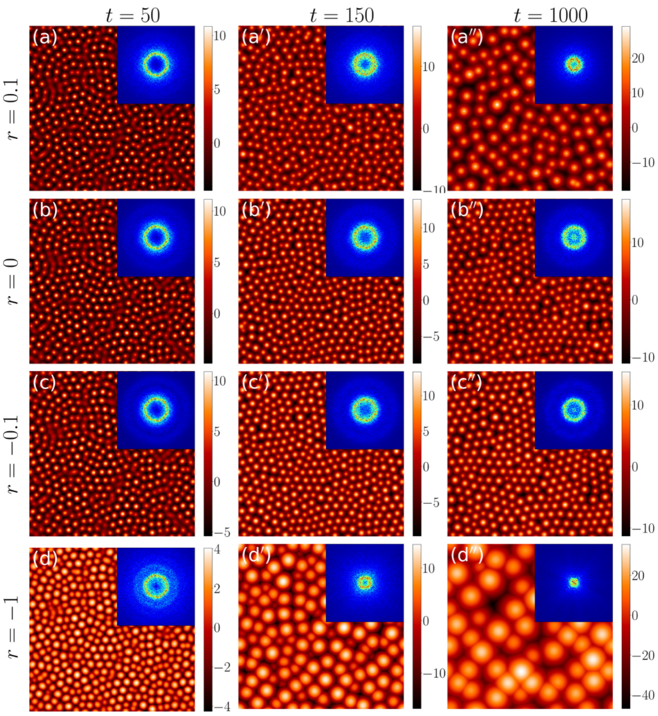

FIG. 5. Simulations of Eq. (50) starting from a low-amplitude spatial noise initial condition for the parameter values $\lambda = 0$ and $\nu = 0.1$. The nonprimed, single prime, and double primes refer to times $t = 50$, $t = 150$, and $t = 1000$, respectively. The values of r were (row a) $r = 0.1$, (row b) $r = 0$, (row c) $r = -0.1$, and (row d) $r = -1$. The insets show the PSD of the surface.

right, $t = 1000$. The rows show snapshots of the surface taken from simulations with different values of the CKS coefficient: $r = 0.1$ in row (a), $r = 0$ in row (b), $r = -0.1$ in row (c), and $r = -1$ in row (d). Although at time $t = 1000$ the surfaces with $r = 0$ and $r = -0.1$, shown in Figs. 5(b″) and 5(c″), respectively, have undergone a similar amount of coarsening and appear to be similar, the dynamics are quite different in the two cases. In the $r = -0.1$ case, the coarsening occurs as some nanodots shrink and then disappear, allowing neighboring nanodots to grow and occupy the area left behind by the now-absent nanodot. On the other hand, in the $r = 0$ case, pairs of nanodots occasionally near one another, collide and coalesce to form one larger nanodot. This coalescence behavior is also observed for $r = 0.1$ [row (a)], but the rate at which it occurs is faster than for $r = 0$. Likewise, the dynamics for $r = -1$ [row (d)] is qualitatively similar to that observed for $r = -0.1$, but more rapid.

The tendency for nanodots to near one another and to coalesce is a consequence of the GCT. To see this, note that the value of F_H' for two widely separated Gaussian protrusions that have volumes V and widths σ is $-2V^3/(4\pi^2\sigma^8) = -V^3/(2\pi^2\sigma^8)$. If these two Gaussians are combined to form a single Gaussian with volume $2V$ and width σ, then F_H' becomes $-(2V)^3/4\pi^2\sigma^8 = -2V^3/\pi^2\sigma^8$. This is four times more negative than the value of F_H' for the two widely separated Gaussians. As a result, we could have anticipated that there would be a tendency for two spikes to near one another and then fuse to form a single spike. The GCT will therefore tend to produce coarsening of the surface morphology.

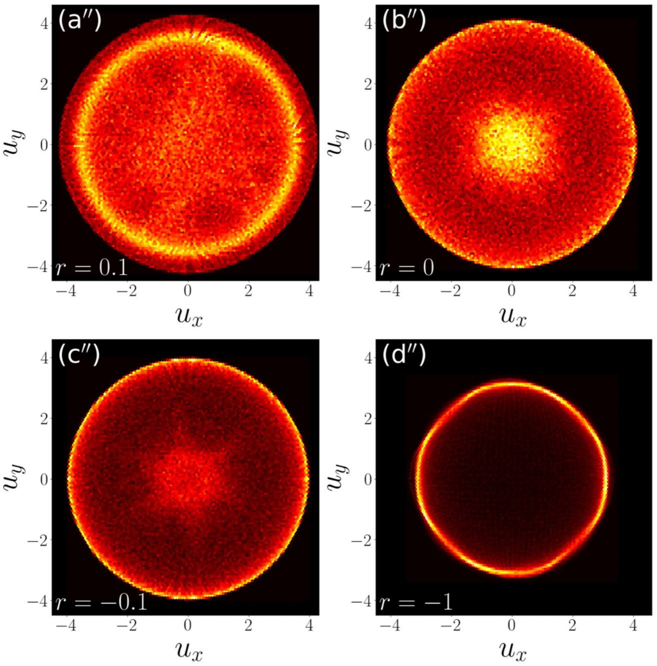

FIG. 6. 2D gradient distributions for panels (a″) - (d″) of Fig. 5. The values of r were (a″) $r = 0.1$, (b″) $r = 0$, (c″) $r = -0.1$ and (d″) $r = -1$.

The CKS nonlinearity $r\nabla^2(\nabla u)^2$ that appears in Eq. (50) is not variational. It is known, however, that it tends to produce coarsening of the surface morphology [37–40]. This term is therefore expected to speed the coarsening that results from the GCT. That is indeed what we see when we compare the behavior for $r = 0.1$ and $r = -1$ with the behavior for $r = 0$ in Fig. 5.

The 2D gradient distributions for Figs. 5(a″)–5(d″) are shown in Fig. 6. In each case, the ES term serves to prevent the formation of high surface slopes, and essentially no values of $|\nabla u|$ are observed beyond a critical value that depends on r. For $r = 0$, there is a pronounced peak centered at $u_x = u_y = 0$. This zero-slope peak is produced by the GCT, which, as we have seen, tends to produce surfaces with sharp peaks separated by flat regions. The peak at $u_x = u_y = 0$ is suppressed to an increasing extent if r is changed from zero, and is entirely absent for $r = -1$, the r value of greatest magnitude represented in Fig. 6. The zero-slope peak is also absent in Fig. 1(c), the 2D gradient distribution for a simulation of Eq. (51), the EOM with no GCT.

B. The intermediate-energy regime

Figure 7 shows the results of a simulation in the intermediate energy regime. The chosen parameter values in Eq. (50) were $\lambda = -0.2$, $r = 0$, and $\nu = 0.05$. As can be seen clearly in the figure, a remarkable degree of hexagonal order develops as time passes. This is evident from both the real-space images of the surface and from the PSDs. The PSDs display both sharp first-order peaks and an impressive number of higher order peaks, both of which are indicative of a very high degree of order. In fact, with these parameters, the surface eventually evolves into a completely defect-free state. This state is shown

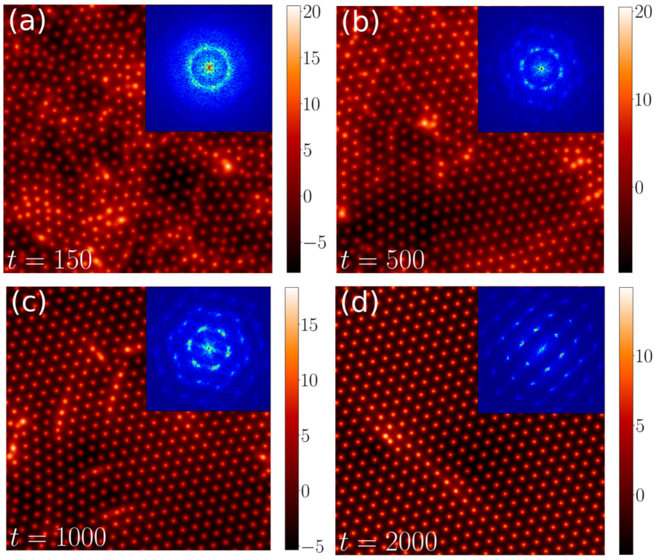

FIG. 7. Results from a simulation of Eq. (50) with $\lambda = -0.2$, $r = 0$, and $\nu = 0.05$ starting from a low-amplitude spatial white noise initial condition. The surface height with the PSD in the insets is shown at times (a) $t = 150$, (b) $t = 500$, (c) $t = 1000$, and (d) $t = 2000$.

in Fig. 8(a). The corresponding PSD, which displays a hexagonal arrangement of narrow peaks, appears in Fig. 8(b).

The development of the hexagonal order seen in Fig. 7 seems to stem in part from an effective repulsion of neighboring nanodots which is caused by the KS nonlinearity $\lambda(\nabla u)^2$. This effective repulsion counterbalances the attraction between nearby nanodots that results from the GCT, and this leads to an increase in the uniformity of the nanodot spacing. In addition, as seen in Fig. 9, a nanodot with significantly larger height than its neighbors will tend to split into two nanodots with reduced height. This tendency is the primary cause for the decreasing surface width seen in Figs. 7(b)–7(d), and it helps to make the nanodot sizes increasingly monodisperse as time passes. Finally, if a pair of nanodots gets too close together, then they may coalesce to form a larger nanodot. Usually, however, this nanodot is short-lived and soon splits into two smaller nanodots, as shown in Fig. 10. Over time, the complex dynamics we have described leads to marked improvements in the hexagonal order.

The presence of the GCT in Eq. (50) plays an essential role in the development of the highly ordered hexagonal arrays of nanodots observed in Fig. 7. To demonstrate this, we simulated Eq. (51) with $\lambda = -0.2$, $r = 0$, and $\nu = 0.05$. This EOM is identical to the equation that yielded Fig. 7, except the GCT is omitted. The result is shown in Fig. 11. No hexagonal order is evident in the real-space images of the surface and, correspondingly, there are no significant peaks in the PSDs aside from the one at the origin. Additionally, the surfaces obtained without the GCT are dominated by rather broad nanoholes rather than localized nanodots.

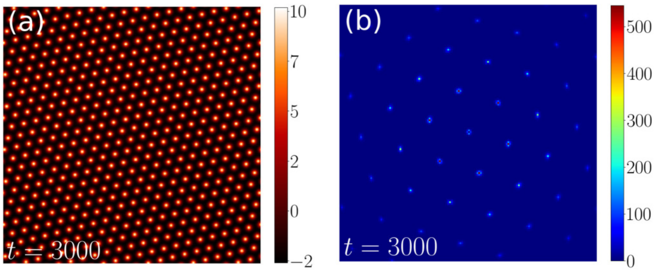

FIG. 8. Results at time $t = 3000$ from a simulation of Eq. (50) with the same parameters as in Fig. 7. The surface height is shown in (a) and the corresponding PSD in (b).

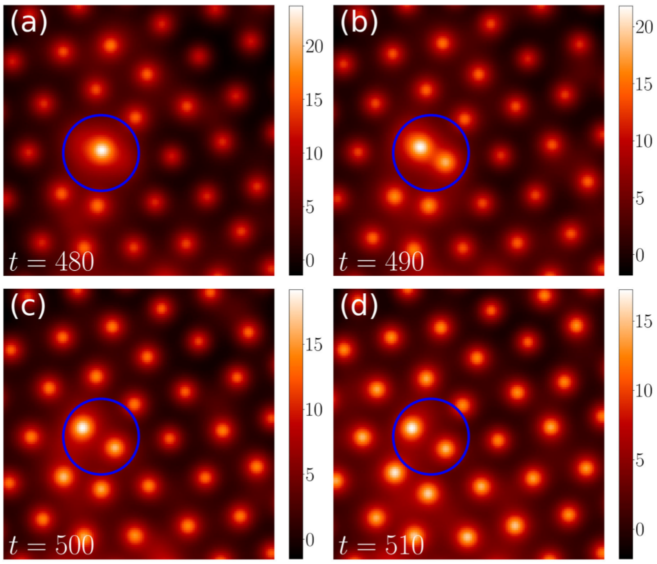

FIG. 9. A zoomed-in view of a simulation with the same parameters used in Fig. 7. The plotted domain has a side length of 47.5. The surface height is shown at times (a) $t = 500$, (b) $t = 510$, (c) $t = 520$, and (d) $t = 530$. Blue circles are included to indicate the region that shows the fission of a nanodot into two nanodots.

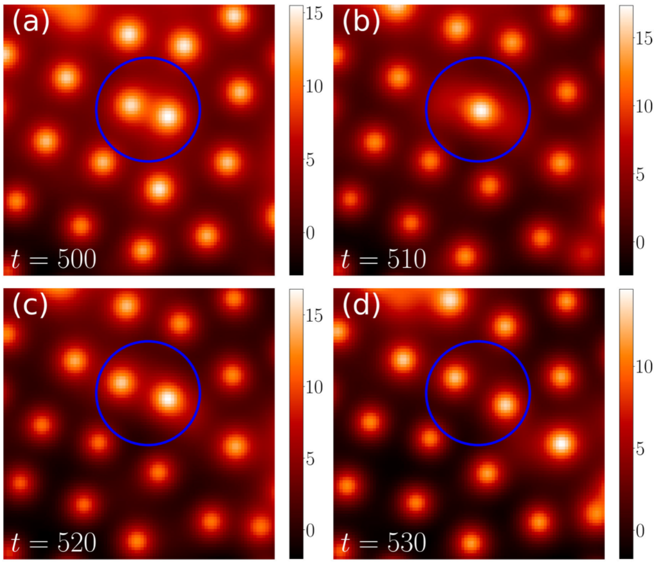

FIG. 10. A zoomed-in view of a simulation with the same parameters used in Fig. 7. The plotted domain has a side length of 32.8. The surface height is shown at times (a) $t = 500$, (b) $t = 510$, (c) $t = 520$, and (d) $t = 530$. Blue circles are included to indicate the region of interest. Two nanodots merge into one between (a) and (b). This nanodot then splits into two between (b) and (c).

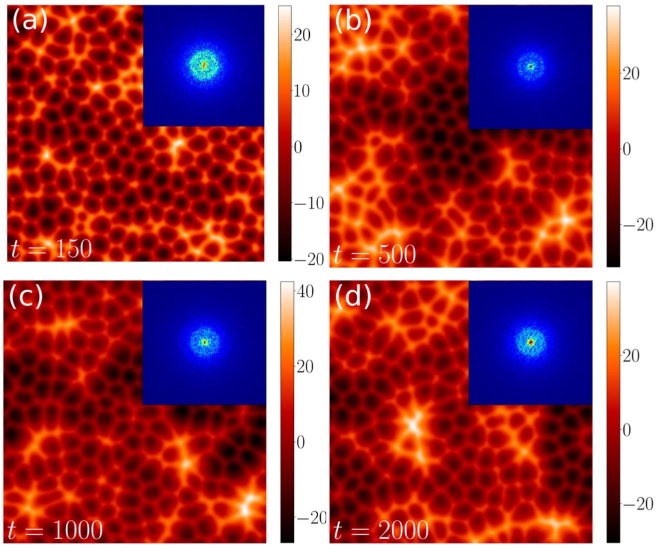

FIG. 11. Results from a simulation of Eq. (51) with $\lambda = -0.2$, $r = 0$, and $\nu = 0.05$ starting from a low-amplitude spatial white noise initial condition. The surface height with the PSD in the insets is shown at times (a) $t = 150$, (b) $t = 500$, (c) $t = 1000$, and (d) $t = 2000$.

The influence of the GCT is also seen in the 2D gradient distributions shown in Fig. 12. The 2D gradient distribution for Fig. 7(d) is shown in Fig. 12(a). This is the result of integrating Eq. (50), which includes the GCT, to time $t = 2000$ with $\lambda = -0.2$, $r = 0$ and $\nu = 0.05$. There is a sharp peak in the 2D gradient distribution centered on the point $u_x = u_y = 0$ and the starlike pattern exhibits clear sixfold symmetry. On the other hand, Fig. 12(b) shows the 2D gradient distribution for Fig. 11(d). This result was obtained with the same values of λ, r and ν as Fig. 12(a), but the simulation was of Eq. (51), which has no GCT. In the absence of the GCT, the peak at zero slope does not appear and there is no sixfold symmetry. This comparison demonstrates the important role that the GCT plays in producing flat regions and reaffirms its role in the emergence of a high degree of hexagonal order.

Nanodot arrays with a high degree of hexagonal order similar to those seen in Fig. 7 form in simulations of Eq. (50) for a range of parameter values. In Fig. 13, the results of four simulations of Eq. (50) with different choices of parameter values are shown at time $t = 2000$.

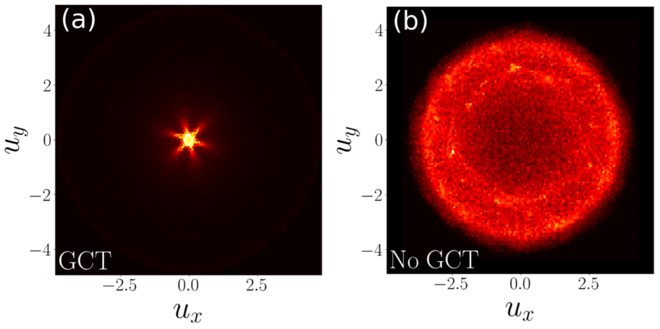

FIG. 12. A comparison of 2D gradient distributions for a simulation with and without the GCT. In (a), the 2D gradient distribution corresponding to Fig. 7(d) is shown. In (b), the 2D gradient distribution corresponding to Fig. 11(d) is shown.

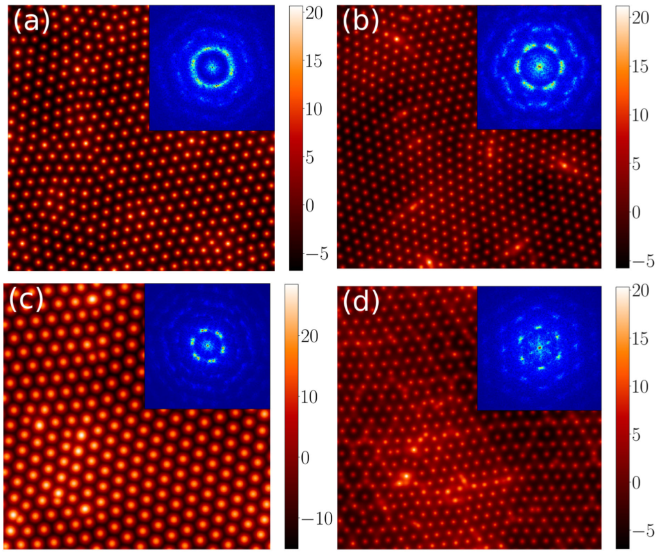

FIG. 13. Results from four simulations of Eq. (50) with different values of λ, r, and ν at time $t = 2000$. The parameter values used were (a) $\lambda = -0.1$, $r = 0$, and $\nu = 0.05$; (b) $\lambda = -0.2$, $r = 0$, and $\nu = 0.04$; (c) $\lambda = -0.2$, $r = 0.3$, and $\nu = 0.04$; and (d) $\lambda = -0.2$, $r = -0.05$, and $\nu = 0.04$.

In Fig. 13(a), the parameter values were $\lambda = -0.1$, $r = 0$, and $\nu = 0.05$. These values resulted in a surface with a high degree of local hexagonal order, but the global hexagonal order is not as strong as in Fig. 7(d), as can be seen from the lack of distinct first-order peaks in the PSD. In this case, regions of hexagonal order separated by grain boundaries are evident in the real-space image of the surface. In simulations in which $r = 0$ and $\nu = 0.05$ and the value of λ was outside the range between -0.3 and zero, the nanodots were disordered.

In Fig. 13(b), the parameter values were $\lambda = -0.2$, $r = 0$, and $\nu = 0.04$. The resulting surface has a high degree of both local and global hexagonal order. The coefficient of the isotropic ES term must be sufficiently small for strong hexagonal order to develop. If $\nu > 0.09$, the resulting surfaces did not exhibit strong hexagonal order. Conversely, as we have seen, if ν is too small, singular spikes form.

In Figs. 13(c) and 13(d), the parameter values were $\lambda = -0.2$, $r = 0.3$, $\nu = 0.04$, and $\lambda = -0.2$, $r = -0.05$, $\nu = 0.04$, respectively. In both cases, there was a nonzero CKS term. If the CKS coefficient is positive, strong local and global hexagonal order developed up to $r = 0.3$. For $r > 0.3$, enhanced local hexagonal order still results, but the size of the nanodots becomes too large to characterize the global order. This is because the larger the value of r, the more coarsening occurs. On the other hand, if r is negative, its magnitude must be quite small for good hexagonal order to develop. For example, in Fig. 13(d), the value of r was -0.05. If $r < -0.1$, then nanoholes form instead of nanodots, and they are not well ordered.

To quantify how the degree of hexagonal order depends on the parameters λ, r, and ν, we performed a persistent homology analysis as described in detail in Refs. [53,54]. In

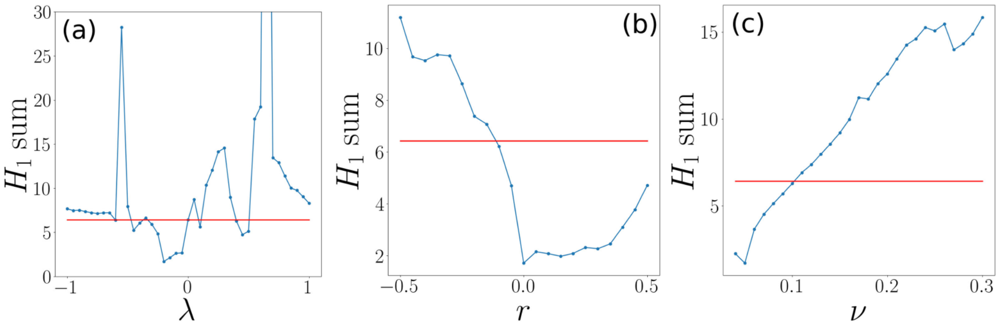

FIG. 14. Normalized H_1 values averaged over times $t = 1900$ to $t = 2000$ for simulations of Eq. (50) in which the three parameters were varied separately. In (a), the values $r = 0$ and $\nu = 0.05$ were fixed while λ ranged from -1 to 1. In (b), the values $\lambda = -0.2$ and $\nu = 0.05$ were fixed while r ranged from -0.5 to 0.5. In (c), the values $\lambda = -0.2$ and $r = 0$ were fixed while ν ranged from 0.04 to 0.3. The red horizontal lines correspond to the normalized H_1 sum for simulations with $r = \lambda = 0$ and $\nu = 0.05$.

this analysis, we first found the xy coordinates of the local maxima of the surface height. We then used these points to calculate the H_1 sum, which, roughly speaking, is a measure of the size of the gaps or "holes" in the hexagonal structure. We then divided the H_1 sum by the number of points. Division by the number of points was carried out to address the issue that some surfaces underwent more coarsening than others, which would cause two equally ordered surfaces to have different raw H_1 scores simply due to the difference in length scale. Finally, we averaged these normalized H_1 sums between the times $t = 1900$ and $t = 2000$ to reduce noise. Lower H_1 scores correspond to a higher degree of hexagonal order [54].

The persistent homology analysis was carried out for simulations in which the parameters λ, r, and ν were varied from the values that led to the well-ordered arrays shown in Fig. 7, i.e., $\lambda = -0.2$, $r = 0$, and $\nu = 0.05$. In Fig. 14(a), the values $r = 0$ and $\nu = 0.05$ were held fixed while λ ranged from -1 to 1 in increments of 0.05. In Fig. 14(b), the values $\lambda = -0.2$ and $\nu = 0.05$ were kept constant while r ranged from -0.5 to 0.5 in increments of 0.05. In Fig. 14(c), ν ranged from 0.04 to 0.3 in increments of 0.01 with the values $\lambda = -0.2$ and $r = 0$ held fixed. The red horizontal lines correspond to the H_1 score for simulations with $r = \lambda = 0$ and $\nu = 0.05$, which we use as a reference case in which a high degree of hexagonal order is lacking.

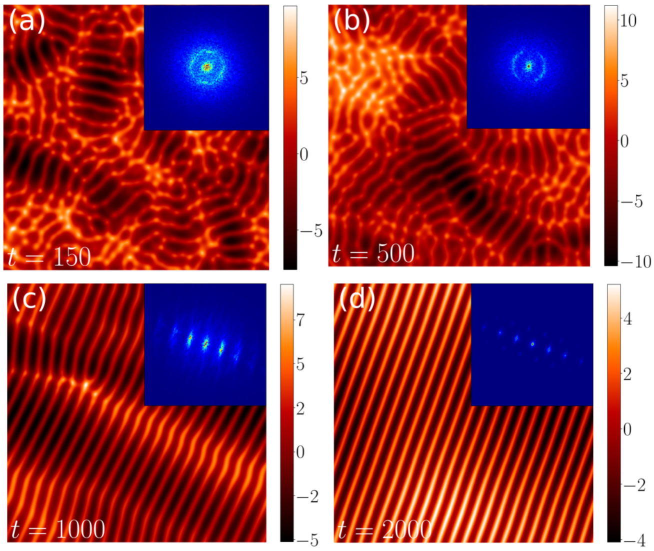

FIG. 15. Results from a simulation of Eq. (50) with $\lambda = -0.55$, $r = 0$, and $\nu = 0.05$ starting from a low-amplitude spatial white noise initial condition. The surface height with the PSD in the insets is shown at times (a) $t = 150$, (b) $t = 500$, (c) $t = 1000$, and (d) $t = 2000$.

The results in Fig. 14(a) show that substantially improved hexagonal ordering is obtained if $-0.2 \leqslant \lambda \leqslant -0.05$ with $r = 0$ and $\nu = 0.05$. Slightly improved order was obtained for $\lambda = 0.45$ and $\lambda = 0.5$, but otherwise positive values of λ led to reduced hexagonal order. There are two interesting upward spikes in the graph at $\lambda = -0.55$ and $\lambda = 0.65$. The large H_1 sum at $\lambda = -0.55$ is due to the formation of well-ordered *ripples* instead of a hexagonal array, as shown in Fig. 15. The H_1 sum was about 100 for $\lambda = 0.65$, but we cut it off this peak in Fig. 14 for clarity. The surface obtained with $\lambda = 0.65$ exhibited unusual dynamics that appear to involve spatiotemporal chaos along with coarsening. The results in Fig. 14(b) show that for $\lambda = -0.2$ and $\nu = 0.05$, improved hexagonal order was obtained for $-0.05 \leqslant r \leqslant 0.5$. Values of r smaller than -0.1 led to reduced hexagonal order. There is no improved hexagonal order in simulations with $\lambda = -0.2$ and $r = 0$ if $\nu \geqslant 0.1$, as shown in Fig. 14(c). In fact, the arrangement of nanodots becomes increasingly disordered as ν is increased beyond 0.1.

V. DISCUSSION AND CONCLUSIONS

We have seen that a term proportional to the Gaussian curvature K appears in the EOM that applies close to the threshold angle for pattern formation θ_c in both the low- and intermediate-energy regimes. The GCT conserves mass, is rotationally invariant, and is variational. The associated effective free energy F'_H makes it energetically advantageous for surface protrusions to grow increasingly high and narrow as time passes and for surface depressions to grow broader and shallower. The GCT also introduces a tendency for protrusions to approach one another and then coalesce, resulting in coarsening of the surface morphology. If its effect is not moderated by an ES term with a sufficiently large coefficient, the GCT leads to the formation of spikes that ultimately become singular.

In the high-energy regime, a term proportional to K does not appear in the EOM that applies for θ just above θ_c.

However, this term could have a significant effect in the high-energy regime if θ is well above θ_c. This possibility was briefly considered in Ref. [42], but was not investigated further.

In traditional, nonrigorous approaches to constructing the EOM in the high-energy regime, one considers u and ∇ to be small and then retains terms up to a selected order in these quantities. The CKS nonlinearity $r\nabla^2(\nabla u)^2$ is frequently included in the EOM, in part because it leads to coarsening, as observed experimentally [1,37–40,43]. The GCT $u_{xx}u_{yy} - u_{xy}^2$ is of the same order in u and ∇ as the CKS nonlinearity. Therefore, if the CKS term is included in the EOM, the GCT must also be included for the sake of consistency. In spite of this, the GCT has universally been omitted from the EOM in studies in which the CKS term is incorporated into the EOM.

It is natural to ask what the origin of the GCT is. It is well-known that the sputter yield of a surface depends on its curvature [2,55]. For oblique incidence bombardment of a rotating sample with ions that have an energy above the sputtering threshold, the leading order correction to the sputter yield that comes from the curvature dependence is proportional to the mean curvature $H \cong \frac{1}{2}\nabla^2 u$. There is also a higher order correction term proportional to $K \cong u_{xx}u_{yy} - u_{xy}^2$ though, and this contributes to the coefficient β in the EOM that applies in the intermediate energy regime, Eq. (49) [42]. The surface mass current $\bar{\boldsymbol{J}}$ is given by Eq. (45). The term $A\boldsymbol{\nabla} u$ is the lowest-order contribution that stems from MR; it is an uphill current if $A > 0$ and downhill if $A < 0$. The term $-\frac{1}{2}\beta(\nabla^2 u)\nabla u$ is a correction to this current, and the prefactor $-\frac{1}{2}\beta(\nabla^2 u)$ plays the role of a mobility. Thus, the mass current due to MR actually depends on the curvature of the surface, and this dependence is encoded in the GCT. The GCT also affects the strength of the CKS nonlinearity because its coefficient β appears in the prefactor of the CKS term $(\beta/4 - r)\nabla(\nabla u)^2$ in $\bar{\boldsymbol{J}}$.

In the intermediate energy regime, the KS nonlinearity $\lambda(\nabla u)^2$ appears in the EOM. This term is not variational, and so there is no effective free energy associated with it. However, the KS nonlinearity acts as if it produces an effective repulsion between nanodots and an approximate steady state with a constant interdot spacing develops in which the GCT and the KS term balance one another. For a range of parameter values, hexagonal arrays of nanodots with an astonishing degree of hexagonal order form. This occurs even though there is a broad band of unstable wavelengths.

Our simulations show that if a rotating elemental material is bombarded with a noble gas ion beam just above the sputter yield threshold and critical angle, highly ordered hexagonal arrays of nanodots may result. This suggests that ion bombardment of an elemental material with concurrent sample rotation could be developed into a viable nanofabrication method. However, significant challenges would have to be overcome. Both the threshold ion energy for sputtering E_c and the threshold angle for pattern formation θ_c would have to be found for the chosen combination of target material and of ion species and energy. E_c could be determined either experimentally or using atomistic simulations. The threshold angle θ_c, on the other hand, would most likely have to be determined experimentally. However, even if an experiment were carried out with E just above E_c and θ just above θ_c, there is no guarantee that the three dimensionless parameters λ, r, and ν in the EOM (50) would turn out to have values that lead to a high degree of hexagonal order. Varying E and θ while still keeping them close to their critical values might be sufficient to identify experimental conditions that would lead to a high degree of order. Alternatively, the values of the parameters could be determined using atomistic simulations and the crater function formalism [33,34,56], and then simulations of Eq. (50) would show whether the chosen values of E and θ lead to an ordered array of nanodots.

Ion bombardment can be used to produce highly ordered arrays of nanodots in other ways besides the one proposed here. Arrays of this kind can, for example, form if certain binary materials are bombarded with a noble gas ion beam [3,4]. In contrast, our method can be used, in principle, for any elemental target material. Highly ordered hexagonal arrays of nanodots have also been observed when an elemental material was bombarded with a beam of nonvolatile ions [5–7] and when impurities were deposited during irradiation of an elemental material with a noble gas ion beam [57,58]. The resulting presence of a second atomic species in a surface layer is undesirable in many applications, however.

Although our proposed method of producing nanodot arrays might prove challenging to implement, our work suggests that it would be fruitful to study the effects of ion bombardment with concurrent sample rotation at low to intermediate ion energies. Experiments of this kind have not yet been carried out and, as we have seen, they are expected to lead to behavior that is not seen at the ion energies that are usually employed.

The data that support the findings of this paper are available from the corresponding author upon reasonable request.

ACKNOWLEDGMENTS

We are grateful to Patrick D. Shipman for valuable discussions. This work was supported by Grant No. DMR-2116753 awarded by the U.S. National Science Foundation.

---

[1] J. Muñoz-García, L. Vázquez, M. Castro, R. Gago, A. Redondo-Cubero, A. Moreno-Barrado, and R. Cuerno, Mater. Sci. Eng. R: Rep. **86**, 1 (2014).

[2] R. M. Bradley and J. M. E. Harper, J. Vac. Sci. Technol. A **6**, 2390 (1988).

[3] S. Facsko, T. Dekorsy, C. Koerdt, C. Trappe, H. Kurz, A. Vogt, and H. L. Hartnagel, Science **285**, 1551 (1999).

[4] F. Frost, A. Schindler, and F. Bigl, Phys. Rev. Lett. **85**, 4116 (2000).

[5] Q. Wei, J. Lian, L. A. Boatner, L. M. Wang, and R. C. Ewing, Phys. Rev. B **80**, 085413 (2009).

[6] M. Fritzsche, A. Muecklich, and S. Facsko, Appl. Phys. Lett. **100**, 223108 (2012).

[7] L. Bischoff, W. Pilz, and B. Schmidt, Appl. Phys. A **104**, 1153 (2011).

[8] L. Bischoff, K.-H. Heinig, B. Schmidt, S. Facsko, and W. Pilz, Nucl. Instrum. Methods Phys. Res., Sect. B **272**, 198 (2012).
[9] R. M. Bradley and P. D. Shipman, Phys. Rev. Lett. **105**, 145501 (2010).
[10] P. D. Shipman and R. M. Bradley, Phys. Rev. B **84**, 085420 (2011).
[11] R. M. Bradley and P. D. Shipman, Appl. Surf. Sci. **258**, 4161 (2012).
[12] A. Zalar, Thin Solid Films **124**, 223 (1985).
[13] E.-H. Cirlin, J. J. Vajo, R. E. Doty, and T. C. Hasenberg, J. Vac. Sci. Technol. A **9**, 1395 (1991).
[14] F. Frost, B. Ziberi, A. Schindler, and B. Rauschenbach, Appl. Phys. A **91**, 551 (2008).
[15] E.-H. Cirlin, J. J. Vajo, and T. Hasenberg, J. Vac. Sci. Technol. B **12**, 269 (1994).
[16] E. Lee, J. Seo, J. Muñoz-García, M. Castro, R. Cuerno, and J.-S. Kim, Phys. Rev. B **105**, 085413 (2022).
[17] R. M. Bradley and E.-H. Cirlin, Appl. Phys. Lett. **68**, 3722 (1996).
[18] R. M. Bradley, Phys. Rev. E **54**, 6149 (1996).
[19] An alternative theory advanced by Lee *et al.* [16] applies in the high flux regime in which a whole layer at the surface of the target is mobilized by the ion impacts and behaves like a highly viscous fluid. Simple dimensional estimates of how high the flux f would have to be for the theory of Lee *et al.* to apply give values orders of magnitude higher than the fluxes used in typical experiments.
[20] T. Basu, D. A. Pearson, R. M. Bradley, and T. Som, Appl. Surf. Sci. **379**, 480 (2016).
[21] A. Metya and D. Ghose, Appl. Phys. Lett. **103**, 161602 (2013).
[22] D. Chowdhury, D. Ghose, and S. A. Mollick, Vacuum **107**, 23 (2014).
[23] D. Chowdhury, D. Ghose, S. A. Mollick, B. Satpati, and S. R. Bhattacharyya, Phys. Status Solidi B **252**, 811 (2015).
[24] A. Lopez-Cazalilla, D. Chowdhury, A. Ilinov, S. Mondal, P. Barman, S. Bhattacharyya, D. Ghose, F. Djurabekova, K. Nordlund, and S. Norris, J. Appl. Phys. **123**, 235108 (2018).
[25] G. Carter and V. Vishnyakov, Phys. Rev. B **54**, 17647 (1996).
[26] M. Moseler, P. Gumbsch, C. Casiraghi, A. C. Ferrari, and J. Robertson, Science **309**, 1545 (2005).
[27] B. Davidovitch, M. J. Aziz, and M. P. Brenner, Phys. Rev. B **76**, 205420 (2007).
[28] H. Hofsäss and O. Bobes, Appl. Phys. Rev. **6**, 021307 (2019).
[29] K. Nordlund (private communication).
[30] The effect that implantation of nonvolatile ions has on the surface dynamics is studied in R. M. Bradley and H. Hofsäss, J. Appl. Phys. **120**, 074302 (2016); H. Hofsäss, K. Zhang, and O. Bobes, *ibid.* **120**, 135308 (2016).
[31] M. Cross and H. Greenside, *Pattern Formation and Dynamics in Nonequilibrium Systems* (Cambridge University Press, Cambridge, England, 2009).
[32] R. M. Bradley and G. Hobler (unpublished).
[33] R. M. Bradley, Phys. Rev. E **102**, 012807 (2020).
[34] R. M. Bradley and T. Sharath, Phys. Rev. E **103**, 022804 (2021).
[35] J. Villain, J. Phys. I **1**, 19 (1991).
[36] L. Golubović, A. Levandovsky, and D. Moldovan, East Asian J. Appl. Math. **1**, 297 (2011).
[37] M. Castro, R. Cuerno, L. Vázquez, and R. Gago, Phys. Rev. Lett. **94**, 016102 (2005).
[38] J. Muñoz-García, M. Castro, and R. Cuerno, Phys. Rev. Lett. **96**, 086101 (2006).
[39] J. Muñoz-García, R. Cuerno, and M. Castro, Phys. Rev. B **78**, 205408 (2008).
[40] T. C. Kim, C.-M. Ghim, H. J. Kim, D. H. Kim, D. Y. Noh, N. D. Kim, J. W. Chung, J. S. Yang, Y. J. Chang, T. W. Noh, B. Kahng, and J.-S. Kim, Phys. Rev. Lett. **92**, 246104 (2004).
[41] M. Raible, S. G. Mayr, S. J. Linz, M. Moske, P. Hänggi, and K. Samwer, Europhys. Lett. **50**, 61 (2000).
[42] R. M. Bradley and G. Hobler, J. Appl. Phys. **129**, 194301 (2021).
[43] J. Muñoz-García, R. Cuerno, and M. Castro, Phys. Rev. E **74**, 050103(R) (2006).
[44] A. A. Golovin, S. H. Davis, and A. A. Nepomnyashchy, Phys. Rev. E **59**, 803 (1999).
[45] A. A. Golovin, A. A. Nepomnyashchy, S. H. Davis, and M. A. Zaks, Phys. Rev. Lett. **86**, 1550 (2001).
[46] See A. J. Bernoff and A. L. Bertozzi, Physica D **85**, 375 (1995), and references therein.
[47] N. C. Overgaard and J. E. Solem, in *International Conference on Scale Space and Variational Methods in Computer Vision* (Springer, Berlin, 2007), pp. 430–441.
[48] W. J. Firey, Mathematika **21**, 1 (1974).
[49] V. Oliker, Indiana Univ. Math. J. **40**, 237 (1991).
[50] B. Andrews, Invent. Math. **138**, 151 (1999).
[51] S. M. Cox and P. C. Matthews, J. Comput. Phys. **176**, 430 (2002).
[52] A.-K. Kassam and L. N. Trefethen, SIAM J. Sci. Comput. **26**, 1214 (2005).
[53] D. A. Pearson, R. M. Bradley, F. C. Motta, and P. D. Shipman, Phys. Rev. E **92**, 062401 (2015).
[54] F. C. Motta, R. Neville, P. D. Shipman, D. A. Pearson, and R. M. Bradley, Physica D **380-381**, 17 (2018).
[55] P. Sigmund, J. Mater. Sci. **8**, 1545 (1973).
[56] M. P. Harrison and R. M. Bradley, Phys. Rev. B **89**, 245401 (2014).
[57] K. Zhang, O. Bobes, and H. Hofsäss, Nanotechnol. **25**, 085301 (2014).
[58] R. Gago, A. Redondo-Cubero, F. J. Palomares, and L. Vázquez, Nanotechnol. **25**, 415301 (2014).